IEEE Access
Multidisciplinary | Rapid Review | Open Access Journal

Received February 2, 2021, accepted March 1, 2021, date of publication March 4, 2021, date of current version March 11, 2021.

Digital Object Identifier 10.1109/ACCESS.2021.3063728

A Novel Versatile Decoupling Structure and Expedited Inverse-Model-Based Re-Design Procedure for Compact Single-and Dual-Band MIMO Antennas

MUHAMMAD ABDULLAH[1] AND SLAWOMIR KOZIEL[1,2], (Senior Member, IEEE)
[1]Engineering Optimization and Modeling Center, Reykjavik University, 101 Reykjavik, Iceland
[2]Faculty of Electronics, Telecommunications and Informatics, Gdańsk University of Technology, 80-233 Gdańsk, Poland

Corresponding author: Slawomir Koziel (koziel@ru.is)

This work was supported in part by the Icelandic Centre for Research (RANNIS) under Grant 206606051, and in part by the National Science Centre of Poland under Grant 2020/37/B/ST7/01448.

ABSTRACT Multiple-input multiple-output (MIMO) antennas are considered to be the key components of fifth generation (5G) mobile communications. One of the challenges pertinent to the design of highly integrated MIMO structures is to minimize the mutual coupling among the antenna elements. The latter arises from two sources, the coupling in the free space and the coupling currents propagating on a ground plane. In this paper, an array of H-shaped parasitic patches is proposed as a decoupling structure for compact MIMO antennas to reduce propagation of the coupling currents on a shared ground plane. The proposed decoupling structure is generic, and it can be applied to different antenna configurations as demonstrated in the work. Furthermore, it is employed to develop a new high-performance compact dual-band MIMO structure featuring acceptable level of element coupling at both operating frequencies. The design is validated both numerically and experimentally. The mutual coupling levels are less than -17 dB and -20 dB, with the total efficiency of 89% and 90%, and the realized gain of 6.6 dB and 7 dB at the two resonant frequencies of 5 GHz and 6 GHz, respectively. Topological complexity of the compact MIMO systems featuring elaborated decoupling structures, a large number of geometry parameters, as well as the necessity of handling multiple performance figures, constitute the major challenges of antenna design, in particular, its re-design for various specifications. To alleviate these difficulties, the paper also provides a procedure for rapid geometry scaling of the dual-band MIMO antennas. Our approach is based on inverse surrogate modeling methods, and results in numerically-derived expressions that enable a precise control over the operating antenna bands within broad ranges thereof (from 4 GHz to 8 GHz for the lower band, and from 1.1 to 1.3 ratio of the upper to lower operating frequency). The aforementioned procedure is accompanied by an optimization-based design refinement scheme. A practical utility of the procedure is corroborated using multiple verification case studies as well as physical measurements of the antenna designed for the exemplary set of performance specifications.

INDEX TERMS Multiple-input multiple-output (MIMO) antennas, decoupling, inverse modeling, isolation, expedited redesign.

I. INTRODUCTION

The world is in the transition phase from the fourth generation (4G) mobile communication technology to the new era of the fifth generation (5G) technology. This necessitates the demands for much broader frequency spectrum and energy efficiency [1]. Without a doubt, multiple-input multiple-output (MIMO) technology has the potential to improve considerably the spectrum efficiency by utilizing multipath propagation. The advantages of MIMO have contributed to its popularity [2]. In certain applications (mobile terminals [3], implantable devices [4], the limited available space requires

The associate editor coordinating the review of this manuscript and approving it for publication was Liangtian Wan.

the utilization of compact MIMO antennas, i.e., the structures featuring inter-element spacing less than half of a wavelength. Tight arrangement of the radiators leads to practical design problems [5]. In particular, strong mutual coupling between the antenna elements results in large voltage standing wave ratio (VSWR), reduced gain and efficiency. These, in turn, become major reasons for a degradation of the MIMO system performance in terms of the reduced channel capacity and signal-to-interference-plus-noise-ratio (SINR) [6]. From the point of view of the symbol error rate, and the MIMO channel capacity, the mutual coupling at the levels not exceeding –15 dB and –17 dB, respectively, is sufficient [7]. However, from the perspective of other performance figures such as out-of-band emission suppression and active voltage standing wave ratio, the mutual coupling well below –17 dB is required [7]. Hence, weak element coupling is a prerequisite for overall good performance of the MIMO systems.

Considerable research efforts have been devoted over the past years towards reduction of mutual coupling in MIMO antennas without physically increasing the inter-element spacing [8]–[21]. One of the representative methods is the employment of defected ground structures (DGSs) [8]–[10], which can efficiently disturb the surface wave propagation between the antenna elements (on a shared ground plane), thus to reduce the mutual coupling levels. However, DGSs cause strong backward radiation from the ground plane, leading to high front-to-back ratio (FBR). This limits the practical usefulness of the DGS technique. Other simple methods to improve element isolation include the use of a neutralization line (NL) [11], independent decoupling network [12], and a T-type decoupling feeding network [13]. Here, the idea is to connect the antenna elements to a decoupling circuit using circuit theory means. The coupling currents between the antenna elements cancel out with the opposite decoupling currents within the network, resulting in improved element isolation. Notwithstanding, employing such networks predominantly causes impedance matching problems along with efficiency degradation due to the added insertion loss. Another concept that has attracted attention of both academia and industry is the use of intrinsically well isolated antenna elements. The decoupling methods based on this idea include polarization and pattern diversity [14]–[18]. Their advantage over the previously discussed techniques is that no additional space is required to insert a decoupling structure. The isolation requirements are fulfilled by incorporating complementary polarizations or radiation patterns of individual antennas. Such decoupling methods are associated with the stringent requirements on the radiating elements and their topologies. Consequently, the use of polarization/pattern diversity methods in practical applications may be limited. Quite recently, artificially created electromagnetic materials emerged as a promising technology for isolation improvement in MIMO antennas. Such materials can be three dimensional (3D) metamaterials, and two dimensional (2D) metasurfaces. Their unique features include, among others, a capability to manipulate the EM waves as per designer requirements [19]. The control over the electromagnetic properties is achieved through the appropriate design of subwavelength periodic arrays of the unit cells. In [20], a dual-band split planar electromagnetic bandgap (EBG) structure has been proposed. It comprises a compact array of metallic patches whose edges are connected to a neighboring patch via a thin meander-line metal strip. The employment of EBG considerably suppresses the propagation of the surface waves, which alleviates the mutual coupling issue. Another way of using metamaterials is to employ a metasurface as a superstrate. In [21], a metasurface superstrate for polarization conversion has been proposed. The metasurface converts the surface wave coupling mode to the orthogonal one. This way, a reduction of mutual coupling can be achieved. Nevertheless, using metasurfaces and metamaterials for isolation improvement significantly increases the overall profile of the device, which hinders the application of this technique for compact MIMO antennas.

The topological complexity of antenna structures featuring low mutual coupling leads to various design difficulties, including the appropriate tuning of geometry parameters. As fulfilling performance requirements pertinent to a specific set of operating conditions is already a challenging endeavor, the majority of the reported MIMO antennas [8]–[21] are designed for particular operating frequencies. No explicit studies are available on how to scale the MIMO designs to other frequencies in a convenient manner. In general, re-design of compact MIMO antennas requires handling of multiple objectives (reflection, isolation, etc.), which itself is a challenging task. Highly non-linear relationships between geometrical and electrical parameters, and the lack of reliable theoretical models only aggravate the problem [22]. As shown in [23], the non-linear relationships between the antenna response and the geometrical parameters can be modeled as an inverse task. In inverse modeling, the target values of electrical and field properties (derived from EM-simulated antenna response) become the model inputs, whereas the (optimum) antenna dimensions are the model outputs [24]. Although setting up the inverse model requires certain computational investments, usually in the form of pre-optimized reference designs [25], the scaling process is greatly facilitated as compared to conventional methods, and permits rapid design correction if necessary [26]. The inverse-model based re-design techniques have been successfully applied to geometry scaling of compact microwave passives [25], [26] as well as antennas [27], [28], and seems to be one of the most promising technologies for expedited design of MIMO structures.

The purpose of this work is twofold. First, we propose a novel decoupling structure for compact MIMO antennas, which is in the form of an array of H-shaped parasitic patches designed to suppress the coupling currents on a shared ground plane. The structure is generic in the sense that it can be combined with various radiators, which is demonstrated through the design of several MIMO antennas. This includes a new compact dual-band MIMO structure being another contribution of the paper. The design is validated both numerically

and experimentally, and shown to outperform the state-of-the-art benchmark devices with respect to major electrical and field characteristics (mutual coupling, efficiency). Furthermore, the antenna is low profile and easy to manufacture. The second purpose of the work is the development and implementation of the inverse-modeling-based framework for rapid geometry scaling of dual-band MIMO antennas. Using the proposed antenna structure, we demonstrate that its geometrical parameters can be scaled precisely and at a low computational cost in the broad ranges of the operating frequencies, from 4 GHz to 8 GHz for the lower band, and from 1.1 to 1.3 ratio of the upper to lower operating frequency. The framework is accompanied by an auxiliary optimization-based design refinement scheme involving trust-region gradient search with antenna response Jacobians estimated using rank-one updating formulas.

The technical novelty and the major contributions of this paper can be summarized as follows: (i) the development of a new decoupling structure for compact single- and dual-band MIMO antennas; (ii) the analysis and verification (both numerical and experimental) of the structure as well as demonstration of its versatility through the design of different antenna configurations working at different operating frequencies; (iii) the development of a new high-performance compact dual-band MIMO antenna; (iv) adaptation of an inverse modeling approach [29] for fast re-design (geometry scaling) of dual-band MIMO antennas over broad ranges of the operating frequencies. It should be emphasized that the presented framework is—to the authors knowledge—the first approach proposed in the literature for convenient and precise control of the antenna operating bands (by means of explicit design formulas being an output of the inverse surrogate).

The remaining part of the article is organized as follows. In Section II, the decoupling structure and its operating principles are described and verified through simulations. Section III discusses the geometries of antenna designs considered in this work. Section IV provides experimental validations of the proposed decoupling structure and a new compact dual-band MIMO antenna. Finally, Section V, outlines the inverse-modeling-based framework for rapid redesign of dual-band MIMO antennas along with its numerical and experimental verification. Section VI concludes the paper.

II. PROPOSED DECOUPLING TECHNIQUE

This section introduces the proposed decoupling structure, subsequently (Section III) applied to design several high-performance antenna structures, including a novel dual-band MIMO antenna. We start by explaining the antenna coupling mechanisms, followed by the geometry of the proposed decoupling circuit and explanation of its operating principles.

A. ANTENNA COUPLING CONCEPT

Figure 1 illustrates the schematic of a conventional MIMO antenna. Two H-plane-coupled patch antennas are placed

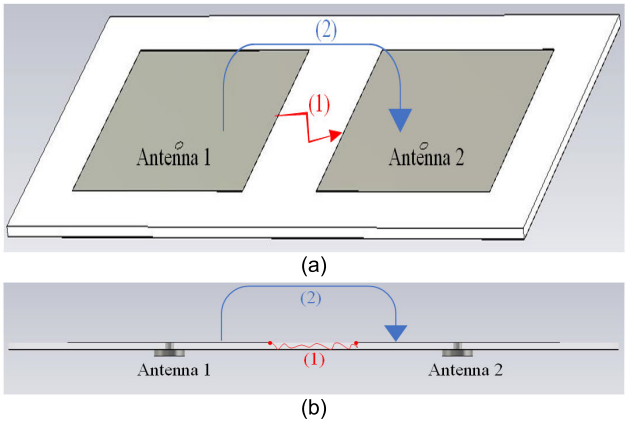

FIGURE 1. Schematic of a MIMO antenna; (1) coupling currents on a ground plane (2) and free space coupling. (a) perspective view (b) side view.

on a shared ground plane. In such an arrangement, exciting Antenna 1 results in coupling the input energy to Antenna 2. There are two primary reasons, i.e., coupling on a ground plane (1), and free-space coupling (2). At the presence of mutual coupling, the antenna patterns alter and they start pointing towards each other (cf. Fig. 2(a)). In the case of closely-spaced uncorrelated antennas (see, e.g., Fig. 5(a)), the mutual coupling tends to make the antenna patterns orthogonal to each other (i.e., the two antennas start radiating in opposite directions). These cases represent the situations that are generally undesired for antenna systems. For example, antenna arrays require elements radiating in the broadside direction (cf. Fig. 2(c)).

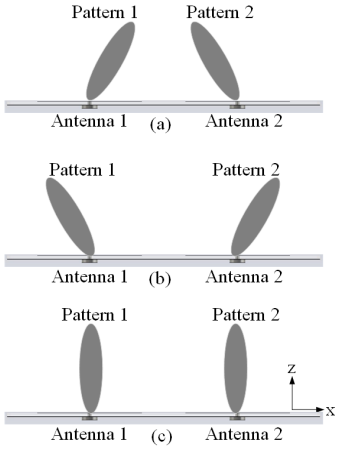

FIGURE 2. Schematic diagram of the antenna beam pattern: (a) correlated antennas, (b) uncorrelated antennas in the presence of mutual coupling, (c) uncorrelated antennas as the elements of an ideal array.

In order to reduce the aforementioned pattern distortion in MIMO antennas it is necessary to suppress the unwanted coupling between the elements. In this work, we attempt to address this issue by suppressing the propagation of the coupling currents on a shared ground plane.

B. PROPOSED DECOUPLING STRUCTURE

The proposed decoupling structure has been shown in Fig. 3. Inspired by [30], the structure consists of periodic arrays of square patches. The metal patches are grounded at the center using 1-mm vias. Note that the number of square patches is not critical. In practice, it is dependent upon the available space between the two antennas, as demonstrated in Section III. To avoid the resonance effect, the neighboring patches are separated by a gap of the size G_1. It assures that the decoupling structure does not affect the antenna radiation pattern.

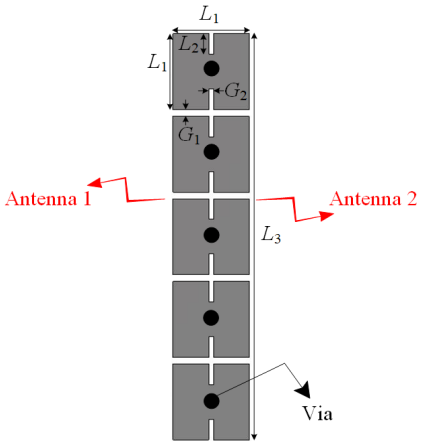

FIGURE 3. Geometry of the proposed decoupling structure.

C. DECOUPLING MECHANISM AND VERIFICATION

To provide an intuitive explanation of the working mechanism of the proposed decoupling structure, the E-field and the surface current distributions are investigated. The decoupling structure is incorporated between the two H-plane coupled antennas (refer to Fig. 6 for more details concerning the antenna configuration). For the analysis, Port 1 is excited and Port 2 is terminated with 50-ohm matching load. The E-field distributions of the MIMO antenna—with and without the decoupling structure—are presented in Fig. 4(a). It can be observed that before applying the decoupling structure, the two antennas are coupled via non-radiating edges, which is known as H-plane coupling. However, upon employing the decoupling circuit, the coupling E-field is confined within the structure, which significantly reduces the strength of the E-field on the terminated patch (Port 2). Similarly, the propagation of the coupling currents on a shared ground plane is noticeably reduced after applying decoupling structure between the two antennas as illustrated in Fig. 4(b). On the contrary, a strong surface wave propagation phenomenon is observed in a MIMO antenna without the decoupling structure.

The same phenomenon can be observed in the case of closely-spaced uncorrelated antennas. The E-field and the surface current distributions are shown in Fig. 5. The explanation is omitted here due to a similar assertion.

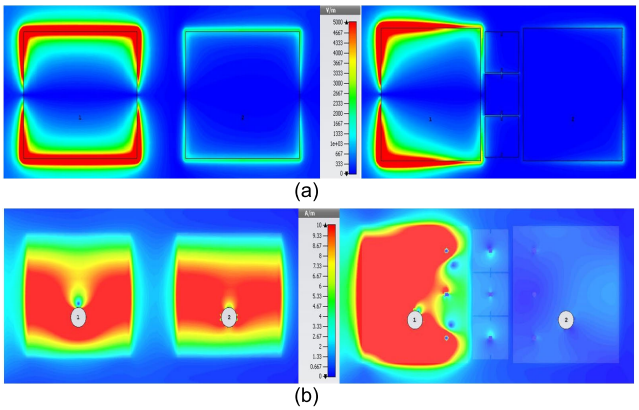

FIGURE 4. The effect of the proposed decoupling concept on the antenna operation: antenna without the decoupling structure (left) and with the decoupling structure (right): (a) E-field distribution (b) surface current distribution.

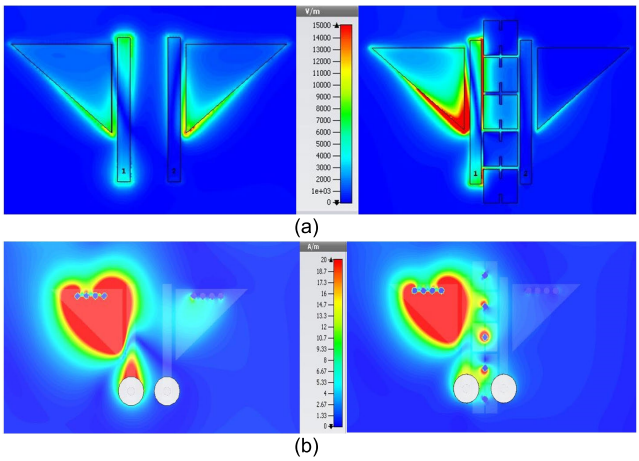

FIGURE 5. Antenna without the decoupling structure (left) and with decoupling structure (right) (a) E-field distribution (b) Surface current distribution.

D. SCATTERING PERFORMANCE AND RADIATION PERFORMANCE

To validate the effectiveness of the proposed decoupling structure, the performance of the MIMO antennas (refer to Fig. 8 for more details concerning the antenna configuration) with and without the decoupling structure is tested. Their reflection and transmission coefficients are shown in Fig. 6. It can be observed that the mutual coupling is reduced from about –13 dB to below –26 dB in the case of correlated antenna elements, and from –12 dB to less than –21 dB in the case of uncorrelated, closely-spaced antenna elements.

Additionally, to demonstrate the effects of the decoupling structure on the radiation performance, the antenna patterns of the two MIMO antennas are also shown in Fig. 7. Due to symmetrical structure, the radiation patterns of only first element (Port 1, see Fig. 8) are presented. It can be observed that upon applying the decoupling structure, the pattern distortion reduces noticeably, and the antennas start radiating in a nearly broadside direction. However, without the decoupling

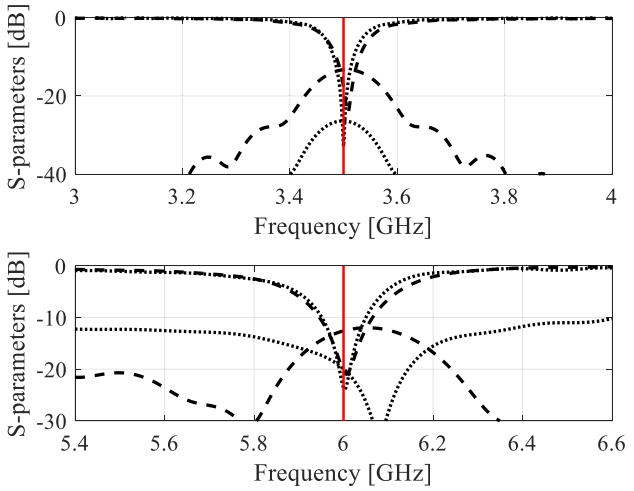

FIGURE 6. Scattering parameters with (· · ··) and without (- - -) the decoupling structure for correlated (top) and uncorrelated (bottom) antenna case. The vertical red line represents the center frequency.

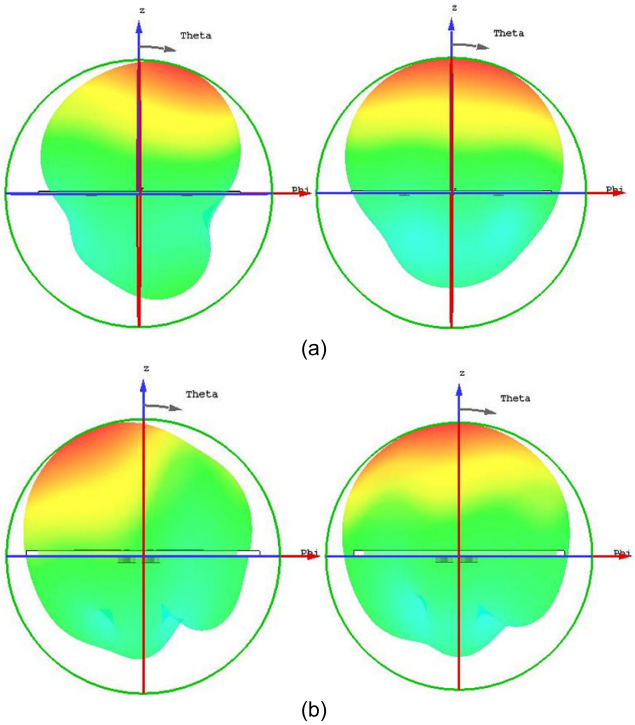

FIGURE 7. Radiation pattern without (left) and with the decoupling structure (right): (a) correlated, and (b) uncorrelated antenna case.

structure, the radiation patterns of correlated antenna elements are pointing towards each other whereas they are in opposite direction (orthogonal) in case of correlated antenna elements. The distinct radiation performance of correlated and uncorrelated antenna without decoupling structure has been explained in Section II.*A*.

The above analysis further validates the efficacy of the proposed decoupling structure. In particular, suppressing the coupling currents allows for considerable reduction of mutual coupling in MIMO antennas.

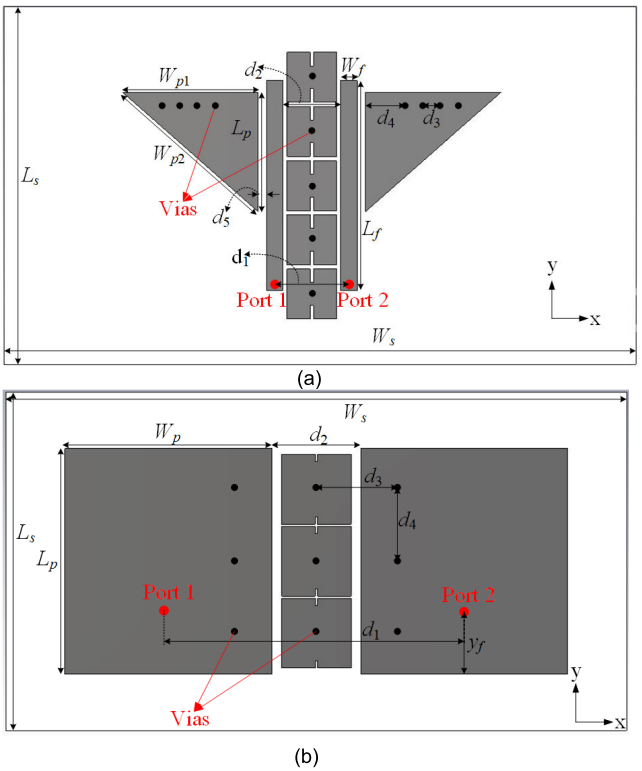

FIGURE 8. Geometries and design parameters of the considered MIMO antennas: (a) Antenna 1, (b) Antenna 2.

The specific data concerning the parameter space (lower/upper bounds) will be provided in Section III. This particular geometry has been chosen in order to ensure sufficient flexibility of the unit cell (cf. Fig. 1(b)) while limiting the number of adjustable parameters (here, three). The latter facilitates the metamodeling-based optimization process, especially the construction of fast surrogate model.

A ground-backed Arlon AD250 lossy substrate ($\varepsilon_r = 2.5$, $h = 1.5$ mm, $\tan\delta = 0.0018$) is used in the unit cell design. During the simulations, metallization is represented as perfect electrical conductor (PEC). The overall size of the unit cell is $W_s \times L_s = 6 \times 6$ mm^2.

It should be noted that the geometries in Fig. 1(b) are for illustration purposes only, and they do not correspond to the final design. Notwithstanding, they are selected to illustrate the unit cell topologies in the assumed parameter space, and, thereby, to demonstrate the topological flexibility of the cell design.

It should be emphasized that the conventional design approaches are not reliable when optimizing such a topology where a small change in the design parameters drastically changes the cell geometry, and, consequently, the reflection phase. This applies to both interactive methods relying on parameter sweeping, but also direct EM-driven optimization techniques, the application of which is hindered by the entailed computational expenses.

III. MODEL DESCRIPTION

This section presents two antenna geometries utilized in this work to illustrate the performance of the proposed decoupling structure. Furthermore, a new compact MIMO antenna is introduced, which exploits the same decoupling concept as well as additional geometry alterations incorporated to enable dual-band operation.

A. SINGLE-BAND MIMO ANTENNAS

Figure 8(a) depicts the geometry of the first MIMO antenna considered in this work (Antenna 1). The bow-shape MIMO structure is implemented on 1.52-mm-thick Arlon AD250 lossy dielectric ($\varepsilon_r = 2.5$, $tan\delta = 0.0018$). The overall dimensions of the antenna are $W_s \times L_s = 45 \times 30$ mm^2. The dimensions of the remaining parameters utilized to manufacture the prototypes will be provided in Section IV. The two elements share a common ground plane on the bottom layer of a substrate. The antenna resonates at 6 GHz, and the two elements are separated by an edge-to-edge distance d_2 of $0.09\lambda_o$, where λ_o is the free space wavelength at 6 GHz. Four shorting vias are allocated on each radiator to match the antenna at a desired frequency.

The second case study (Antenna 2) utilized in this work is shown in Fig. 8(b). It is a conventional rectangular shape MIMO antenna featuring the proposed decoupling structure between the two patches. This antenna is implemented on a Rogers RO4350B lossy dielectric ($\varepsilon_r = 3.48$, $tan\delta = 0.0037$, $h = 0.81$ mm). The overall size of the ground plane is $W_s \times L_s = 72 \times 39$ mm^2. The antenna resonates at 3.5 GHz frequency and the two elements are separated by an edge-to-edge distance $d_2 = 0.1\lambda_o$.

B. DUAL-BAND MIMO ANTENNA

Figure 9 depicts the geometry of a novel dual-band high-isolation MIMO antenna implemented on Arlon AD250 lossy dielectric ($\varepsilon_r = 2.5$, $tan\delta = 0.0018$, $h = 1.52$ mm). The antenna dimensions are $W_s \times L_s = 69 \times 29$ mm^2. The operating frequencies of the antenna are 5 GHz and 6 GHz. The two elements are separated by an edge-to-edge distance $d_2 = 0.06\lambda_o$, (here, λ_o is the free space wavelength at 5 GHz). The three 1-mm-diameter vias are introduced near the coupled edges of two antennas to raise the resonant frequency of the second order mode [31]. The decoupling structure is inserted between the gap present in the vicinity of the non-radiating edges. The four corners of a rectangular patches are rounded and expurgated to further enhance isolation at the upper resonant frequency.

All antennas are excited by 50Ω input ports allocated behind the ground plane. Throughout this work, full wave EM simulation software, CST Microwave Studio, is utilized for antenna performance analysis, whereas the parameter optimization process is realized using MATLAB R2018a and Matlab-to-CST socket to communicate with the EM solver.

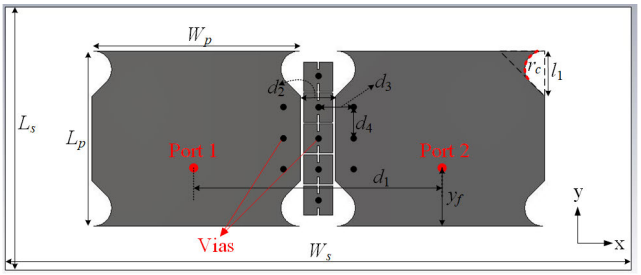

FIGURE 9. Configuration of the proposed dual-band MIMO antenna $\{r_c = l_1/2.5\}$.

IV. EXPERIMENTAL VALIDATIONS

To demonstrate the efficacy of the decoupling structure for practical MIMO antennas, a case study will be considered in this section. The application example is the convectional rectangular-shape MIMO antenna resonating at 3.5 GHz (Antenna 2). Furthermore, the performance of a new compact dual-band MIMO antenna is discussed in detail, and benchmarked against the state-of-the-art designs. All antennas are simulated using CST Microwave Studio. Antenna 1 and the dual-band structure are fabricated using standard printed circuit board technology (PCB). The optimized dimensions of the designs can be found in Table 1.

TABLE 1. Geometry parameters of Considered MIMO Antenna Designs.

Geometry parameters (mm)		
Antenna 1	Antenna 2	Dual-band MIMO Antenna
W_{p1}=11.46	W_p=24.18	W_p=23.1
W_{p2}=15.23	L_p=26.29	L_p=19.3
L_p=10.03	y_f=8.24	y_f=5.55
L_f=17.66	d_1=34.55	d_1=26.97
W_f=1.41	d_2=10.37	d_2=3.87
d_1=6.26	d_3=10.04	d_3=5.42
d_2=4.86	d_4=8.39	d_4=3.42
d_3=1.50	L_1=8.13	L_1=3.22
d_4=2.73	L_2=0.83	L_2=0.82
L_1=4.20	L_3=24.90	L_3=16.92
L_2=1.14	G_1=0.26	G_1=0.2
L_3=22.44	G_2=0.26	G_2=0.2
G_1=0.36		l_1=4.99
G_2=0.27		r_c=1.99

A. SINGLE-BAND MIMO ANTENNAS

Figure 10 shows the photographs of a single-band MIMO antenna prototype. For practical measurements, the antenna elements are fed via 50-ohm SMA connectors. The electrical and field performance of the antennas has been measured in an anechoic chamber of Reykjavik University. While characterizing the antenna excited at one of the ports, the other port has been terminated with 50-ohm matching load.

The comparison between the simulated and measured reflection and transmission coefficients are presented in Fig. 11. A measured mutual coupling is below –25 dB for

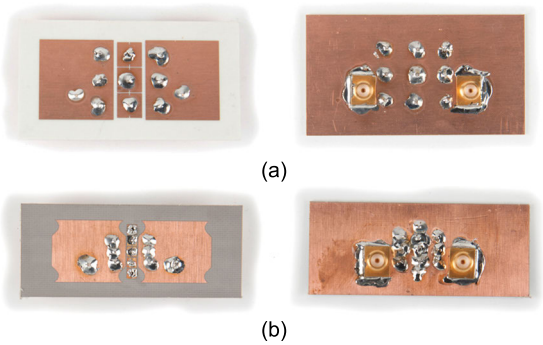

FIGURE 10. Photographs of the top (left) and bottom (right) side of the antenna prototypes: (a) Antenna 2; (b) novel dual-band MIMO antenna.

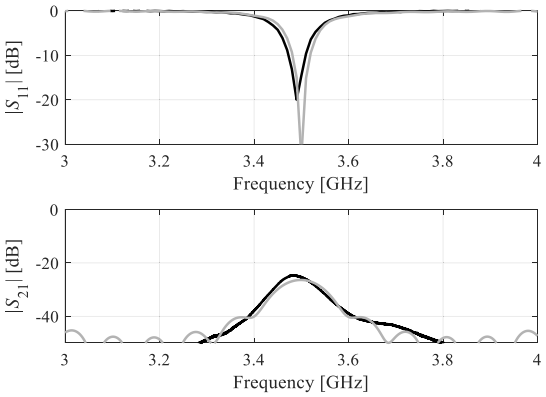

FIGURE 11. Measured (black) and simulated (gray) scattering parameters of Antenna 2.

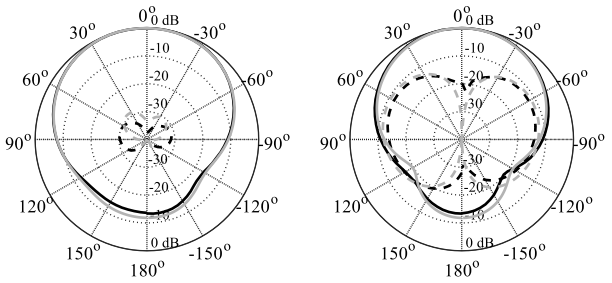

FIGURE 12. Co- (solid line) and cross-polarized (dotted line) radiation patterns of Antenna 2 in the H-plane (left) and E-plane (right). Simulation results (gray) and measurements (black).

Antenna 2 at a resonant frequency. Furthermore, the co- and cross-polarized normalized radiation patterns of Antenna 2 are shown in Fig. 12. A good agreement between the simulation and measurement results can be observed.

B. DUAL-BAND MIMO ANTENNA

Configuration of the proposed compact dual-band MIMO antenna has been shown in Fig. 9, whereas the photograph of the manufactured prototype can be found in Fig. 10(b). The performance of a dual-band MIMO antenna has been demonstrated in Figs. 13 through 16. Due to the symmetrical structure of the device, only the results for Port 1 being active are presented; nevertheless, the antenna exhibits similar performance when excited at Port 2.

The comparison between the simulated and measured scattering parameters are presented in Fig. 13. It can be noticed that the measured mutual coupling level is below –17 dB and –20 dB at 5 GHz and 6 GHz, respectively. A slight disagreement at a higher resonant frequency in terms of reflection performance is due to the manual implementation of vias and the soldering effects.

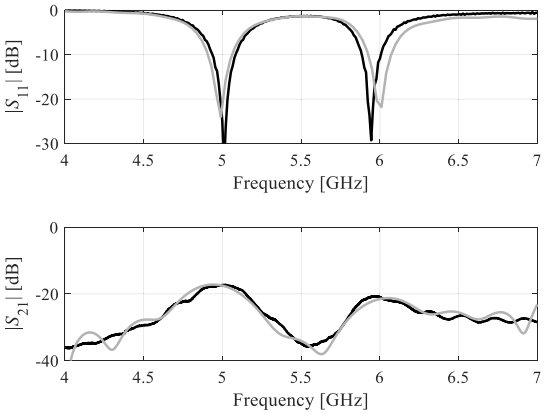

FIGURE 13. Scattering parameter performance of a dual-band MIMO antenna. Simulation results (gray) and measurements (black).

The simulated and measured normalized radiation patterns of a proposed dual-band MIMO antenna at the corresponding operating frequencies, in both *xoz*- and *yoz*-plane (cf. Fig. 9) are shown in Fig. 14. As depicted, the measurements agree well with simulations in terms of both co- and cross-polarized patterns. The higher cross-polarization level (in the orthogonal direction) at 6 GHz in the *yoz*-plane can be attributed to the excitation of the orthogonal mode component of the patch antenna to realize dual-band operation. Still, the cross polarization level towards the maximum radiation direction, i.e., about 0°, is below –15 dB.

Figure 15 demonstrates the comparison between the simulated and measured realized antenna gain. The measured maximum gain is 6.6 dBi and 7 dBi at 5 GHz and 6 GHz, respectively. A slight discrepancy between simulated and measured gain can be observed, which can be attributed to the fabrication tolerances, nevertheless, the overall trend in the gain variation agrees well with the simulations. The efficiency of a dual-band MIMO antenna is depicted in Fig 16. Owing to limited amenities, the experimental characterization of the efficiency was not possible. However, considering a good agreement between simulations and measurements in terms of radiation patterns and gain performance, it is safe to conclude that the proposed dual-band MIMO antenna exhibits similar level of agreements in the case of total efficiency as well.

For the sake of benchmarking, the proposed compact dual-band MIMO antenna has been compared with the recently reported state-of-the-art designs, see Table 2. It should be emphasized that apart from proposing the novel

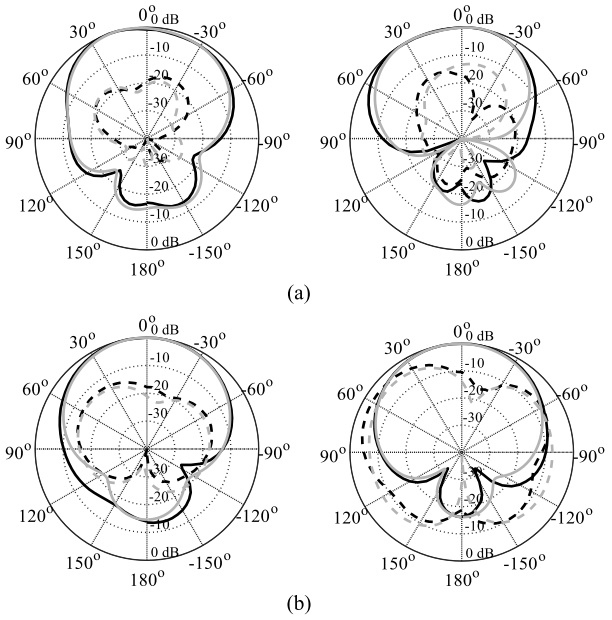

FIGURE 14. Co- (solid line) and cross-polarized (dotted line) radiation patterns at 5 GHz (left) and 6 GHz (right) of a dual-band MIMO antenna: (a) H-plane (xz), (b) E-plane (yz). Simulation results (gray) and measurements (black).

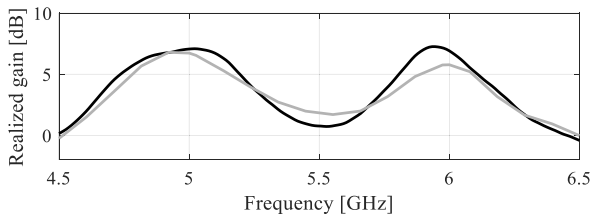

FIGURE 15. Measured (black) and simulated (gray) realized gain of a dual-band MIMO antenna.

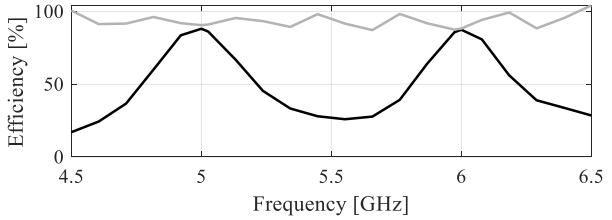

FIGURE 16. Total (black) and radiation (gray) efficiency of a dual-band MIMO antenna.

antenna design, explicit design formulas developed using the inverse-modeling-based framework are also provided in this work. These sort of formulas—presented in the literature for the first time—allow for convenient re-design of the antenna for different operating conditions. The re-design technique will be discussed in detail in Section V. Below, the comparison is carried out in terms of isolation level, realized gain, total efficiency, and edge-to-edge spacing between the antenna elements. The data in Table 2 indicates that the proposed antenna outperforms the other designs with respect to total efficiency as well as realized gain. It can also be

TABLE 2. Proposed Antenna With the State-of-art Dual-Band MIMO Antennas.

Ref	Edge-to-edge spacing	Worst coupling level (dB)	Worst Total Efficiency	Worst Realized Gain (dBi)
[36]	0.15 λ_o	–20.3	70%	-
[37]	0.24 λ_o	–13.5	70%	1.7
[38]	0.2 λ_o	–17.2	-	5.0
[39]	0.04 λ_o	–20.0	-	3.0
[40]	0.1 λ_o	–15.1	-	1.0
[9]	0.2 λ_o	–15.0	80%	-
Proposed	0.01 λ_o	–17.3	89%	6.6

observed that with the mutual coupling levels almost comparable, the edge-to-edge spacing between the elements of the proposed MIMO antenna is the smallest among the considered cases, which improves the compactness of the proposed structure. Overall, the proposed dual-band MIMO antenna seems to be an attractive alternative to the existing solutions.

V. INVERSE MODELING & NUMERICAL ANALYSIS

This section outlines a simple procedure for rapid dimension scaling of MIMO antennas. It adopts the methodology of [29], which employs the inverse surrogate model as its main component. It is followed by the correction procedure to account for the surrogate inaccuracy, and the accelerated gradient-based refinement algorithm for final tuning of the antenna parameters. The procedure is formulated and its operation is illustrated for the case of dual-band MIMO antenna but it is generic and can be applied for single-band cases as well. The section is concluded by verification case studies, i.e., antenna re-design for several target operating frequencies.

A. DIMENSION SCALING OF DUAL-BAND MIMO ANTENNA. PROBLEM FORMULATION

The task is to redesign a dual-band MIMO antenna (cf. Fig. 7) so that it operates at required center frequencies. The scaling of antenna geometry parameters is to be carried out at a low computational cost. The figures of interest are the operating frequency f_1 of the lower band and the operating frequency of the upper band $f_2 = \alpha f_1$, where α is a scaling factor. The vector of antenna geometry parameters, and the response of the EM simulation model will be denoted as $\boldsymbol{x} \in R^n$, and $\boldsymbol{R}(\boldsymbol{x})$, respectively. We also denote as $\boldsymbol{x}_f^*(f_1, \alpha)$ the antenna parameter vector optimized for the frequencies f_1 and $f_2 = \alpha f_1$. The optimum is understood here as the solution to the following constrained problem:

$$\boldsymbol{x}_f^*(f_1, \alpha) = \arg\min_{\boldsymbol{x}} \{\max\{|S_{11}(\boldsymbol{x}, f_1)|, |S_{11}(\boldsymbol{x}, \alpha f_1)|\} \quad (1)$$

subject to $|S_{21}(\boldsymbol{x},f_1)| \leq -15$ dB and $|S_{21}(\boldsymbol{x},\alpha f_1)| \leq -15$ dB, where $S_{k1}(\boldsymbol{x},f)$, $k = 1, 2$, is the value of the respective S-parameter at the design $\boldsymbol{x}$ and frequency f. The re-design task is to identify $\boldsymbol{x}_f^*(f_1, \alpha)$ for any given f_1 and α within a specified range $f_{1.\min} \leq f_1 \leq f_{1.\max}$ and $\alpha_{\min} \leq \alpha \leq \alpha_{\max}$.

B. GEOMETRY SCALING USING INVERSE SURROGATES

We adopt the methodology of [29], where the scaling process is facilitated by the use of the inverse surrogate model that produces approximation of $\boldsymbol{x}_f^*(f_1, \alpha)$ given f_1 and α as the model inputs. The inverse model is constructed using a set of reference designs pre-optimized for the pairs $[f_{1.j}, \alpha_j]$, $j = 1,\ldots, N$. For the sake of computational efficiency, the reference designs are obtained using feature-based optimization procedure [32].

The inverse model $\boldsymbol{x}_s(f_1, \alpha)$ is set up individually for each geometry parameter. We have

$$\boldsymbol{x}_s(f_1, \alpha, \boldsymbol{P}) = \left[x_{s.1}(f_1, \alpha, \boldsymbol{p}_1) \ \ldots \ x_{s.1}(f_1, \alpha, \boldsymbol{p}_n)\right]^T \quad (2)$$

where $x_{s.l}(f_1, \alpha, \boldsymbol{p}_l)$ is a model of the lth geometry parameter; $\boldsymbol{p}_l$ stand for the model coefficients; $\boldsymbol{P} = [\boldsymbol{p}_1 \ \ldots \boldsymbol{p}_n]$ is the overall (aggregated) vector of the inverse model coefficients. Here, the following analytical formulation of the inverse model in used:

$$x_{s.l}(f_1, \alpha) = q(f_1, \alpha) s_{f_1}(f_1) s_\alpha(\alpha) \quad (3)$$

where

$$s_{f_1}(f_1) = a_1 + a_2 \exp(a_3 f_1) \quad (4)$$
$$s_\alpha(\alpha) = a_4 + a_5 \exp(a_6 \alpha) \quad (5)$$
$$q(f_1, \alpha) = a_7 + a_8 f_1 + a_9 \alpha \quad (6)$$

Following [29], the exponential curves are utilized to model the relationship between the operating frequencies and geometry parameters, whereas the linear term q accounts for joint effects of the operating frequencies.

Inverse model identification is realized by solving the following nonlinear regression problem

$$\boldsymbol{p}_l = \arg\min_{\boldsymbol{p}} \sum_{j=1}^{N} \left(x_{s.l}(f_{1.j}, \alpha_j) - x_{s.j.l}\right)^2 \quad (7)$$

where $\boldsymbol{x}_{s.j} = [x_{s.j.1} \ldots x_{s.j.n}]^T$ is the reference design corresponding to the operating frequencies $f_{1.j}$ and $\alpha_j f_{1.j}$, $j = 1$, …, N. It is generally recommended [29] that the number of reference designs is at least equal to the number of model coefficients in order to avoid overfitting of the regression model as well as identifying the dominant trends in the data.

The parameters of the antenna re-designed to given target operating frequencies f_{t1} and $f_{t2} = \alpha_t f_{t1}$ can be obtained as

$$\boldsymbol{x}_f^*(f_{t1}, \alpha_t) = \boldsymbol{x}_s(f_{t1}, \alpha_t, \boldsymbol{P}) \quad (8)$$

In practice, the formula (8) yields a good initial design, which may exhibit certain deviations $\Delta f_1 = f_{t1} - f_{a1}$ and $\Delta\alpha = \alpha_t - \alpha_a$ between the target and the actual operating frequencies f_{a1} and $f_{a2} = \alpha_a f_{a1}$. These deviations can be accommodated to produce an improved design as

$$\boldsymbol{x}_f^*(f_{t1}, \alpha_t) = \boldsymbol{x}_s(f_{t1} + \Delta f_1, \alpha_t + \Delta\alpha, \boldsymbol{P}) \quad (9)$$

The cost of this correction is just one EM simulation of the antenna structure under design [29].

C. DESIGN REFINEMENT BY FAST GRADIENT SEARCH

The scaling procedure described in Section III.*B* can only control the frequency location of the antenna resonances, therefore, some final tuning may be required to improve the resonance depths as well as correct the isolation response S_{21}. In this work, it is realized using the trust-region (TR) gradient search algorithm [33]. The problem is formulated as

$$\boldsymbol{x}^* = \arg\min_{\boldsymbol{x}} U(\boldsymbol{R}(\boldsymbol{x}), f_1, \alpha) \quad (10)$$

with the objective function U defined as

$$U(\boldsymbol{R}(\boldsymbol{x}), f_1, \alpha) = \max\{|S_{11}(\boldsymbol{x}, f_1)|, |S_{11}(\boldsymbol{x}, \alpha f_1)|\} + \beta c_S(\boldsymbol{x}, f_1, \alpha)^2 \quad (11)$$

where $c_S(\boldsymbol{x}, f_1, \alpha) = \max\{\max\{|S_{21}(\boldsymbol{x}, f_1)|, |S_{21}(\boldsymbol{x}, \alpha f_1)|\} + 15, 0\}/15$ is a penalty function that quantified violation of the condition $|S_{21}| \leq -15$ dB (at both operating bands). The coefficient β controls the contribution of the penalty term. The TR algorithm produces a series of approximations $\boldsymbol{x}^{(j)}$, $j = 0, 1, \ldots,$ to $\boldsymbol{x}^*$ as (here, $\boldsymbol{x}^{(0)} = \boldsymbol{x}_f^*(f_{t1}, \alpha_t)$ produced by (9))

$$\boldsymbol{x}^{(j+1)} = \arg\min_{\boldsymbol{x};\ \boldsymbol{x}^{(j)} - \boldsymbol{d}^{(j)} \leq \boldsymbol{x} \leq \boldsymbol{x}^{(j)} - \boldsymbol{d}^{(j)}} U(\boldsymbol{L}^{(j)}(\boldsymbol{x}), f_1, \alpha) \quad (12)$$

where

$$\boldsymbol{L}^{(j)}(\boldsymbol{x}) = \boldsymbol{R}(\boldsymbol{x}^{(j)}) + \boldsymbol{J}_{\boldsymbol{R}}(\boldsymbol{x}^{(j)}) \cdot (\boldsymbol{x} - \boldsymbol{x}^{(j)}) \quad (13)$$

is a linear expansion model of $\boldsymbol{R}$ at $\boldsymbol{x}^{(j)}$. The Jacobian matrix $\boldsymbol{J}_{\boldsymbol{R}}$ is estimated using finite differentiation in the first iteration. Subsequently, it is updated using the Broyden formula [34], [35], which is sufficient because the initial design is already close to the optimum. By using the Broyden update, the refinement cost can be kept low, to about $2n$ EM antenna simulations, where n is the number of antenna parameters. The size vector $\boldsymbol{d}^{(j)}$ is adjusted adaptively using the standard TR rules [33].

D. REDESIGN OF COMPACT DUAL-BAND MIMO ANTENNA

The procedure of Sections V.*B–C* is utilized to redesign the compact dual-dual band MIMO antenna of Fig. 9, see also Section III.*B*. The structure is implemented on a 1.52-mm-thick Arlon AD250 dielectric substrate ($\varepsilon_r = 2.5$; $\tan\delta = 0.0018$). The vector of designable parameters are $[L_p\ L_r\ W_{pr}\ G_2\ y_{fr}\ d_{2r}\ L_{1r}\ d_{3r}\ l_{1r}\ L_{2r}]^T$; the parameters with subscript r are relative variables. The following relations hold: $L_r = L_p + L_r$, L_r is the offset to the length of the patch L_p, $W_p = W_{pr}(L_p/0.8 - L_p/1.2) + 1.2L_p$, $y_f = y_{fr}(L_p/8 - L_p/2) + L_p/2$, $d_2 = d_{2r}(L_p/3.5 - L_p/5) + L_p/5$, $L_1 = L_{1r}(L_p/4 - L_p/6) + L_p/6$, $d_3 = d_{3r}(L_p/3.5 - L_p/5) + L_p/5$, $l_1 = l_{1r}(L_p/3 - L_p/4) + L_p/4$, $L_2 = L_{2r}((L_p - 1) - L_p/4) + L_p/4$. The unit for the absolute variables is mm. The lower and upper design variable bounds are $\boldsymbol{l} = [8\ {-2}\ 0\ 0\ 0.2\ 0\ 0\ 0\ 0\ 0\ 0]^T$ and $\boldsymbol{u} = [50\ 5\ 1.0\ 0.7\ 1.0\ 1.0\ 1.0\ 1.0\ 1.0\ 1.0]^T$. The EM model is evaluated using the time domain solver of CST Microwave Studio.

The intended re-design ranges are $4 \leq f_1 \leq 8$ and $1.1 \leq \alpha \leq 1.3$. Nine reference designs are employed, allocated on a uniform 3×3 grid within the aforementioned ranges, i.e.,

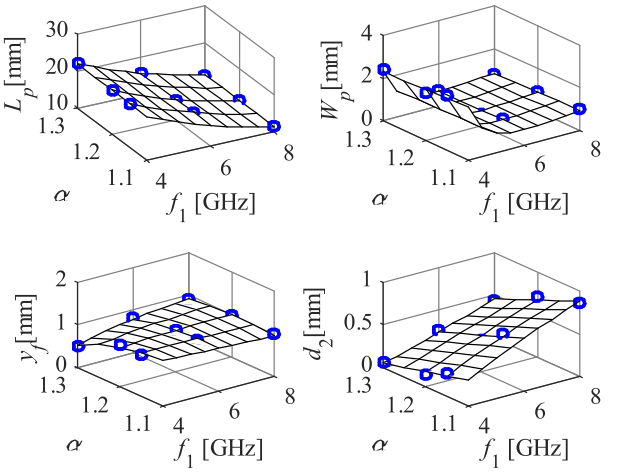

FIGURE 17. Graphical illustration of the inverse surrogate constructed for the dual band MIMO antenna, here, shown for selected geometry parameters: geometry parameter values at the reference designs (o) and the inverse model (—).

TABLE 3. Geometry Parameters of The Verification Design Cases.

Geometry parameters (mm)	Design specifications $\{f_1 f_2\}$ [GHz]			
	{4 4.9}	{6 7.2}	{6.6 8.2}	{8 10.4}
L_p	21.89	15.40	13.90	11.36
L_r	2.27	0.65	0.65	0.76
W_{pr}	0.83	0.99	0.99	0.89
G_2	0.38	0.21	0.43	0.65
y_{fr}	0.11	0.39	0.36	0.44
d_{2r}	0.10	0.33	0.27	0.18
L_{1r}	0.25	0.82	0.74	0.73
d_{3r}	0.41	0.01	0.23	0.52
l_{1r}	0.53	0.11	0.1	0.26
L_{2r}	0.67	0.89	0.40	0.19

TABLE 4. Inverse Modeling Results: Target and Actual Operating Frequencies at Various Re-design Stages.

Target operating frequencies [GHz]		Inverse model output		After first correction		After fine tuning	
f_1	f_2	f_1	f_2	f_1	f_2	f_1	f_2
4.0	4.9	3.97	4.81	4.00	4.91	4.00	4.90
6.0	7.2	5.97	7.28	6.01	7.24	5.99	7.20
6.6	8.2	6.54	8.16	6.60	8.20	6.6	8.20
8.0	10.4	7.88	10.12	7.98	10.30	7.99	10.40

for all combinations of the pairs $f_1 \in \{4.0, 6.0, 8.0\}$ GHz and $\alpha \in \{1.1, 1.2, 1.3\}$. The inverse surrogate is constructed as in Section V.*C*. Figure 17 shows the graphical illustration of the surrogate for the selected antenna parameters. The numerical details concerning the inverse model coefficients can be found in Appendix A.

Practical application of the procedure as well as its numerical verification has been arranged by re-designing the

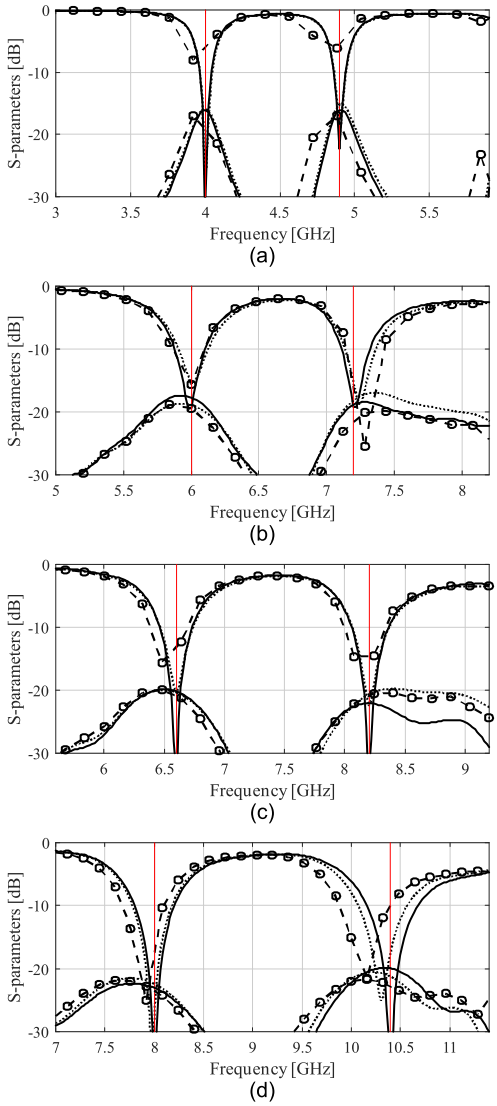

FIGURE 18. Reflection and transmission characteristics for the antenna of Section III.B redesigned for four target pairs of operating frequencies: (a) {4 4.9}, (b) {6.0 7.2}, (c) {6.6 8.2}, and (d) {8.0 10.4} (frequencies in GHz). The vertical lines represent the target operating frequencies: design obtained directly from the inverse surrogate (o), design upon the first stage of correction (· · · ·), and the final design obtained after the second correction (refinement) stage (—).

dual-band MIMO antenna for several pairs of target operating frequencies: $\{f_1\ f_2\}$ GHz (i) {4 4.9}, (ii) {6.0 7.2}, (iii) {6.6 8.2}, and (iv) {8.0 10.4}. The geometry parameters extracted upon applying the procedure of Section V are given in Table 3. The inverse modeling results are gathered in Table 4, whereas as the responses evaluated using EM simulation model are shown in Fig. 18. The detailed information about the re-design formulas, including the values of the inverse model coefficients, can be found in Appendix A. It can be observed that the quality of the design obtained directly from the inverse model is already good. The first correction stage (cf. (9)) noticeably improves the alignment of the center frequencies with the target operating frequencies,

e.g., for the first and the fourth verification design case. The refinement procedure (cf. Section V.*C*) ensures precise matching of the design to the target operating frequencies. At the same time, it enforces the mutual coupling level to remain below –15 dB (recall, that the inverse modeling only takes care of the frequency relationships but it does not directly handles the S_{21} characteristic).

Overall, the verification cases demonstrate both the reliability and the efficacy of the presented re-design procedure. In particular, it allows for a precise control over the operating frequencies of dual-band MIMO antenna. On the other hand, it is computationally efficient. The cost of generating a nearly optimum design, i.e., that one obtained after the first correction stage, is only one EM simulation of the antenna. The overall cost of the redesign process is only between fifteen to eighteen EM simulations of the antenna design, which is negligible considering the range of the target operating frequencies covered by the re-design domain and the number of geometry parameters to be adjusted. It should be noted that in this paper, we only described the inverse modelling procedure of a dual-band MIMO antenna. However, this procedure can be easily adopted to other cases, including the single-band designs presented in Section III.*A*.

VI. CONCLUSION

In this article, a novel decoupling structure has been proposed to suppress coupling currents on a shared ground plane in the MIMO antenna configuration. Its performance has been validated both numerically and experimentally by applying it to two single- and one dual-band MIMO antenna structures. The measurement results indicate that the proposed decoupling structure improves the isolation performance by about 12 to 15 decibels, compared to the antennas without the decoupling structure. It is also shown that the presented approach allows for minimizing the distortion of antenna radiation patterns being a result of unwanted coupling. Furthermore, utilizing the aforementioned decoupling structure, a novel compact high-performance dual-band MIMO antenna is proposed. The reflection and radiation performance of the new design has been experimentally verified, and benchmarked against the state-of-the-art devices from the literature. The dual-band MIMO antenna features the mutual coupling lower than –17 dB and –20 dB, with the total efficiency of 89% and 90%, and the realized gain of 6.6 dB and 7 dB, at its resonant frequencies of 5 GHz and 6 GHz, respectively. Additionally, the inverse-modeling-based framework has been developed for rapid geometry scaling of dual-band MIMO antennas. It has been demonstrated that the proposed antenna design can be scaled precisely in the broad ranges of the operating frequencies, from 4 GHz to 8 GHz for the lower band, and from 1.1 to 1.3 ratio of the upper-to-lower operating frequency. Therewithal, the computational cost of the scaling procedure remains low, i.e., a few EM simulations of the structure at hand.

The presented study demonstrates a practical utility of inverse surrogate modeling in the context of precise dimension scaling of compact single- and dual-band MIMO antennas. Due to the structural complexity and the presence of a considerable number of designable variables, allocating the operating frequencies of such antennas at the required values is a serious challenge, let alone antenna re-tuning for other sets of operating conditions. The framework adopted in this work is a promising algorithmic solution that greatly facilitates the optimization and re-design of compact MIMO structures.

One of the objectives of the future work will be extension of the proposed decoupling method to large scale arrays, as well as generalization of the surrogate-assisted methodology to rapid geometry scaling of such systems.

APPENDIX A

Here, the numerical values of the inverse model coefficients a_k, $k = 1, \ldots, 9$, (cf. (3)-(6)), considered in Section V and applied to re-design the dual-band MIMO antenna, are provided.

TABLE 5. Coefficients Of The Inverse Model (3)-(6) Applied to Dual-Band MIMO Antenna Geometry Scaling.

Design variables	a_1	a_2	a_3	a_4	a_5
L_p	1.38	0.70	1.89	0.13	3.70
L_r	3.79×10^{-4}	8.55	2.56	0.001	15.67
W_{pr}	0.98	0.03	–0.81	0.24	1.53
G_2	5.3×10^{-4}	0.46	2.46	0.99	0.79
y_{fr}	1.02	0.04	–0.89	1.28	–5.52
d_{2r}	1.79×10^{-4}	1.78	–5.07	–2.31	3.07
L_{1r}	2.23	–0.22	–0.33	–0.10	–0.005
d_{3r}	1.39×10^{-4}	–0.74	7.38	–0.51	–27.53
l_{1r}	3.81×10^{-4}	–0.08	0.93	0.41	2.68
L_{2r}	0.92	–0.05	–0.41	0.26	3.08×10^{-5}

Design variables	a_6	a_7	a_8	a_9
L_p	–0.31	1.75	2.07	–0.52
L_r	–2.05	7.69	19.15	–1.19
W_{pr}	–0.24	–3.15	0.94	2.06
G_2	–0.76	0.68	–0.77	–0.20
y_{fr}	–0.59	1.16	1.01	–2.52
d_{2r}	–0.02	–0.80	2.73	–0.81
L_{1r}	1.01	2.26	–0.83	0.98
d_{3r}	–1.42	1.28	–0.40	1.01
l_{1r}	–0.57	–0.32	1.84	–0.65
L_{2r}	1.25	1.84	0.10	3.37

REFERENCES

[1] E. G. Larsson, O. Edfors, F. Tufvesson, and T. L. Marzetta, "Massive MIMO for next generation wireless systems," *IEEE Commun. Mag.*, vol. 52, no. 2, pp. 186–195, Feb. 2014.
[2] X. Chen and S. Zhang, "Multiplexing efficiency for MIMO antenna-channel impairment characterisation in realistic multipath environments," *IET Microw., Antennas Propag.*, vol. 11, no. 4, pp. 524–528, Mar. 2017.
[3] K. Fujimoto and K. Itoh, *Antennas for Small Mobile Terminals*. Boston, MA, USA: Artech House, 2018.
[4] K. Bazaka and M. Jacob, "Implantable devices: Issues and challenges," *Electronics*, vol. 2, no. 4, pp. 1–34, Dec. 2012.

[5] M. S. Sharawi, "Printed multi-band MIMO antenna systems and their performance metrics [Wireless Corner]," *IEEE Antennas Propag. Mag.*, vol. 55, no. 5, pp. 218–232, Oct. 2013.
[6] X. Chen, S. Zhang, and Q. Li, "A review of mutual coupling in MIMO systems," *IEEE Access*, vol. 6, pp. 24706–24719, Apr. 2018.
[7] S. Zhang, X. Chen, and G. F. Pedersen, "Mutual coupling suppression with decoupling ground for massive MIMO antenna arrays," *IEEE Trans. Veh. Technol.*, vol. 68, no. 8, pp. 7273–7282, Aug. 2019.
[8] C. Kumar, M. I. Pasha, and D. Guha, "Defected ground structure integrated microstrip array antenna for improved radiation properties," *IEEE Antennas Wireless Propag. Lett.*, vol. 16, pp. 310–312, May 2017.
[9] Q. Li, M. Abdullah, and X. Chen, "Defected ground structure loaded with meandered lines for decoupling of dual-band antenna," *J. Electromagn. Waves Appl.*, vol. 33, no. 13, pp. 1764–1775, Jul. 2019.
[10] K. Wei, J.-Y. Li, L. Wang, Z.-J. Xing, and R. Xu, "Mutual coupling reduction by novel fractal defected ground structure bandgap filter," *IEEE Trans. Antennas Propag.*, vol. 64, no. 10, pp. 4328–4335, Oct. 2016.
[11] S. Zhang and G. F. Pedersen, "Mutual coupling reduction for UWB MIMO antennas with a wideband neutralization line," *IEEE Antennas Wireless Propag. Lett.*, vol. 15, pp. 166–169, May 2016.
[12] M. Li, L. Jiang, and K. L. Yeung, "Novel and efficient parasitic decoupling network for closely coupled antennas," *IEEE Trans. Antennas Propag.*, vol. 67, no. 6, pp. 3574–3585, Jun. 2019.
[13] X.-J. Zou, G.-M. Wang, Y.-W. Wang, and H.-P. Li, "An efficient decoupling network between feeding points for multielement linear arrays," *IEEE Trans. Antennas Propag.*, vol. 67, no. 5, pp. 3101–3108, May 2019.
[14] M.-Y. Li, Y.-L. Ban, Z.-Q. Xu, G. Wu, C.-Y.-D. Sim, K. Kang, and Z.-F. Yu, "Eight-port orthogonally dual-polarized antenna array for 5G smartphone applications," *IEEE Trans. Antennas Propag.*, vol. 64, no. 9, pp. 3820–3830, Sep. 2016.
[15] M. Li, Z. Xu, Y. Ban, C. Sim, and Z. Yu, "Eight-port orthogonally dual-polarised MIMO antennas using loop structures for 5G smartphone," *IET Microw., Antennas Propag.*, vol. 11, no. 12, pp. 1810–1816, Sep. 2017.
[16] M. Abdullah, Q. Li, W. Xue, G. Peng, Y. He, and X. Chen, "Isolation enhancement of MIMO antennas using shorting pins," *J. Electromagn. Waves Appl.*, vol. 33, no. 10, pp. 1249–1263, Apr. 2019.
[17] C. F. Ding, X. Y. Zhang, C.-D. Xue, and C.-Y.-D. Sim, "Novel pattern-diversity-based decoupling method and its application to multielement MIMO antenna," *IEEE Trans. Antennas Propag.*, vol. 66, no. 10, pp. 4976–4985, Oct. 2018.
[18] K. Saurav, N. K. Mallat, and Y. M. M. Antar, "A three-port polarization and pattern diversity ring antenna," *IEEE Antennas Wireless Propag. Lett.*, vol. 17, no. 7, pp. 1324–1328, Jul. 2018.
[19] S. Sun, Q. He, J. Hao, S. Xiao, and L. Zhou, "Electromagnetic metasurfaces: Physics and applications," *Adv. Opt. Photon.*, vol. 11, no. 2, pp. 380–479, 2019.
[20] X. Tan, W. Wang, Y. Wu, Y. Liu, and A. A. Kishk, "Enhancing isolation in dual-band meander-line multiple antenna by employing split EBG structure," *IEEE Trans. Antennas Propag.*, vol. 67, no. 4, pp. 2769–2774, Apr. 2019.
[21] M. Li, B. G. Zhong, and S. W. Cheung, "Isolation enhancement for MIMO patch antennas using near-field resonators as coupling-mode transducers," *IEEE Trans. Antennas Propag.*, vol. 67, no. 2, pp. 755–764, Feb. 2019.
[22] S. Koziel and A. Pietrenko-Dabrowska, "Performance-based nested surrogate modeling of antenna input characteristics," *IEEE Trans. Antennas Propag.*, vol. 67, no. 5, pp. 2904–2912, May 2019.
[23] S. Koziel and A. Bekasiewicz, "Inverse surrogate modeling for low-cost geometry scaling of microwave and antenna structures," *Eng. Comput.*, vol. 33, no. 4, pp. 1095–1113, Jun. 2016.
[24] C. Zhang, J. Jin, W. Na, Q.-J. Zhang, and M. Yu, "Multivalued neural network inverse modeling and applications to microwave filters," *IEEE Trans. Microw. Theory Techn.*, vol. 66, no. 8, pp. 3781–3797, Aug. 2018.
[25] S. Koziel and A. Bekasiewicz, "Expedited geometry scaling of compact microwave passives by means of inverse surrogate modeling," *IEEE Trans. Microw. Theory Techn.*, vol. 63, no. 12, pp. 4019–4026, Dec. 2015.
[26] S. Koziel and A. Bekasiewicz, "Computationally-efficient surrogate-assisted dimension scaling of compact dual-band couplers," *IET Microw., Antennas Propag.*, vol. 11, no. 4, pp. 465–470, Mar. 2017.
[27] S. Koziel and A. Bekasiewicz, "Rapid dimension scaling for notch frequency redesign of UWB band-notch antennas," *J. Electromagn. Waves Appl.*, vol. 30, no. 17, pp. 2280–2292, Nov. 2016.
[28] S. Koziel, A. Bekasiewicz, and L. Leifsson, "Rapid EM-driven antenna dimension scaling through inverse modeling," *IEEE Antennas Wireless Propag. Lett.*, vol. 15, pp. 714–717, Mar. 2016.
[29] S. Koziel and A. Pietrenko-Dabrowska, "Inverse surrogates for accelerated simulation-driven design," in *Performance-Driven Surrogate Modeling of High-Frequency Structures*. Cham, Switzerland: Springer, 2020, pp. 341–390.
[30] K.-L. Wu, C. Wei, X. Mei, and Z.-Y. Zhang, "Array-antenna decoupling surface," *IEEE Trans. Antennas Propag.*, vol. 65, no. 12, pp. 6728–6738, Dec. 2017.
[31] M. Abdullah, X. Chen, and Q. Li, "On the resonant frequencies of dual-band patch antennas," *Electron. Lett.*, vol. 55, no. 7, pp. 368–370, Apr. 2019.
[32] S. Koziel, "Fast simulation-driven antenna design using response-feature surrogates," *Int. J. RF Microw. Comput.-Aided Eng.*, vol. 25, no. 5, pp. 394–402, Jun. 2015.
[33] A. R. Conn, N. I. M. Gould, and P. L. Toint, *Trust Region Methods* (MPS-SIAM Series on Optimization). Philadelphia, PA, USA: SPIE, 2000.
[34] C. G. Broyden, "A class of methods for solving nonlinear simultaneous equations," *Math. Comput.*, vol. 19, no. 92, pp. 577–593, 1965.
[35] S. Koziel, J. W. Bandler, and Q. S. Cheng, "Robust trust-region space-mapping algorithms for microwave design optimization," *IEEE Trans. Microw. Theory Techn.*, vol. 58, no. 8, pp. 2166–2174, Aug. 2010.
[36] M. E. Ouahabi, A. Zakriti, M. Essaaidi, A. Dkiouak, and E. Hanae, "A miniaturized dual-band MIMO antenna with low mutual coupling for wireless applications," *Prog. Electromagn. Rec. C*, vol. 93, pp. 93–101, 2019.
[37] N. Pouyanfar, C. Ghobadi, J. Nourinia, K. Pedram, and M. Majidzadeh, "A compact multi-band MIMO antenna with high isolation for C and X bands using defected ground structure," *Radioengineering*, vol. 27, no. 3, pp. 686–693, Sep. 2018.
[38] V. Satam and S. Nema, "Defected ground structure planar dual element MIMO antenna for wireless and short range RADAR application," in *Proc. IEEE Int. Conf. Signal Process., Informat., Commun. Energy Syst. (SPICES)*, Kozhikode, India, Feb. 2015, pp. 1–5.
[39] P. Liu, D. Sun, P. Wang, and P. Gao, "Design of a dual-band MIMO antenna with high isolation for WLAN applications," *Prog. Electromagn. Rec. Lett.*, vol. 74, pp. 23–30, Feb. 2018.
[40] A. Chaudhari and R. K. Gupta, "Dual-band MIMO antenna structures with high isolation," in *Proc. IEEE Region 10 Conf. (TENCON)*, Kochi, India, Oct. 2019, pp. 230–234.

MUHAMMAD ABDULLAH received the B.Sc. degree from the University of Engineering and Technology, Pakistan, in 2016, and the M.Sc. degree from Xi'an Jiaotong University (XJTU), China, in 2019. Since 2019, he has been associated with the Department of Engineering, Reykjavik University, Iceland, as a Researcher. From 2018 to 2019, he was with the Electromagnetics and Communication Laboratory, XJTU. His broader research interests include surrogate-based modeling and optimization, CAD and modeling of antennas and other high-frequency structures, simulation-driven design, machine-learning techniques, and millimeter-wave communication. He received the Excellent Master's Thesis Award on completion of M.Sc. degree.

SLAWOMIR KOZIEL (Senior Member, IEEE) received the M.Sc. and Ph.D. degrees in electronic engineering from the Gdansk University of Technology, Poland, in 1995 and 2000, respectively, the M.Sc. degrees in theoretical physics and in mathematics, in 2000 and 2002, respectively, and the Ph.D. degree in mathematics from the University of Gdansk, Poland, in 2003. He is currently a Professor with the Department of Engineering, Reykjavik University, Iceland. His research interests include CAD and modeling of microwave and antenna structures, simulation-driven design, surrogate-based optimization, space mapping, circuit theory, analog signal processing, evolutionary computation, and numerical analysis.